

Non-stationary dynamo and magnetospheric accretion processes of the classical T Tauri star V2129 Oph

J.-F. Donati^{1*}, J. Bouvier², F.M. Walter³, S.G. Gregory⁴, M.B. Skelly¹, G.A.J. Hussain⁵, E. Flaccomio⁶, C. Argiroffi⁷, K.N. Grankin⁸, M.M. Jardine⁹, F. M enard², C. Dougados², M.M. Romanova¹⁰ & the MaPP collaboration

¹ *LATT-UMR 5572, CNRS & Univ. de Toulouse, 14 Av. E. Belin, F-31400 Toulouse, France*

² *LAOG-UMR 5571, CNRS & Univ. J. Fourier, 414 rue de la Piscine, F-38041 Grenoble, France*

³ *Department of Physics and Astronomy, Stony Brook University, Stony Brook NY 11794-3800, USA*

⁴ *School of Physics, Univ. of Exeter, Stocker Road, Exeter EX4 4QL, UK*

⁵ *ESO, Karl-Schwarzschild-Str. 2, D-85748 Garching, Germany*

⁶ *INAF, Osservatorio Astronomico di Palermo, Piazza del Parlamento 1, 90134 Palermo, Italy*

⁷ *DSFA, Univ. di Palermo, Piazza del Parlamento 1, 90134 Palermo, Italy*

⁸ *Crimean Astrophysical Observatory, Nauchny, Crimea 334413, Ukraine*

⁹ *School of Physics and Astronomy, Univ. of St Andrews, St Andrews, Scotland KY16 9SS, UK*

¹⁰ *Department of Astronomy, Cornell University, Ithaca, NY 14853-6801, USA*

2010 November, MNRAS in press

ABSTRACT

We report here the first results of a multi-wavelength campaign focussing on magnetospheric accretion processes of the classical T Tauri star (cTTS) V2129 Oph. In this paper, we present spectropolarimetric observations collected in 2009 July with ESPaDOnS at the Canada-France-Hawaii Telescope (CFHT) and contemporaneous photometry secured with the SMARTS facility. Circularly polarised Zeeman signatures are clearly detected, both in photospheric absorption and accretion-powered emission lines, from time-series of which we reconstruct new maps of the magnetic field, photospheric brightness and accretion-powered emission at the surface of V2129 Oph using our newest tomographic imaging tool – to be compared with those derived from our old 2005 June data set, reanalyzed in the exact same way.

We find that in 2009 July, V2129 Oph hosts octupolar and dipolar field components of about 2.1 and 0.9 kG respectively, both tilted by about 20° with respect to the rotation axis; we conclude that the large-scale magnetic topology changed significantly since 2005 June (when the octupole and dipole components were about 1.5 and 3 times weaker respectively), demonstrating that the field of V2129 Oph is generated by a non-stationary dynamo. We also show that V2129 Oph features a dark photospheric spot and a localised area of accretion-powered emission, both close to the main surface magnetic region (hosting fields of up to about 4 kG in 2009 July). We finally obtain that the surface shear of V2129 Oph is about half as strong as solar.

From the fluxes of accretion-powered emission lines, we estimate that the observed average logarithmic accretion rate (in $M_{\odot} \text{ yr}^{-1}$) at the surface of V2129 Oph is -9.2 ± 0.3 at both epochs, peaking at -9.0 at magnetic maximum. It implies in particular that the radius at which the magnetic field of V2129 Oph truncates the inner accretion disc is $0.93\times$ and $0.50\times$ the corotation radius (where the Keplerian period equals the stellar rotation period) in 2009 July and 2005 June respectively.

Key words: stars: magnetic fields – stars: formation – stars: imaging – stars: rotation – stars: individual: V2129 Oph – techniques: spectropolarimetry

1 INTRODUCTION

Magnetic fields are thought to play an important role during the formation of stars and their planetary systems. In

* E-mail: donati@ast.obs-mip.fr

particular, they presumably oppose the collapse of the giant molecular clouds from which stars and planets form, strongly inhibit its fragmentation into multiple globules, efficiently evacuate most of the accreting mass (e.g., through conical outflows and collimated jets) and rapidly dissipate the initial reservoir of angular momentum (e.g., André et al. 2008); they also likely affect the formation and migration of planets in the accretion discs surrounding newly-born stars.

The impact of magnetic fields on the formation of low-mass stars (i.e., with $M_* \leq 3 M_\odot$) that are still surrounded with a gaseous accretion disc – the so-called classical T Tauri stars or cTTSs – has been the subject of intense scrutiny and vivid debates in the last two decades. With their intense large-scale fields, cTTSs are putatively capable of braking the inner regions of their accretion discs and of braking their rotation rather drastically, although the exact physical process through which they can reach this result is still controversial (e.g., Bouvier et al. 2007, for a review).

Following several papers reporting the presence of strong fields on cTTSs (e.g., Johns-Krull 2007), the first spectropolarimetric studies based on time-series of Zeeman signatures from accreting and non-accreting regions at the surfaces of cTTSs revealed that low-mass protostars indeed possess large-scale fields, but that the intensity and topologies of their fields strongly depend on the protostellar mass in a way very reminiscent to those of low-mass main-sequence stars (Donati et al. 2007, 2008a; Donati & Landstreet 2009; Donati et al. 2010a). These initial results however call for a confirmation through surveys on a statistically significant sample of cTTSs, allowing in particular to study how the properties of their large-scale magnetic fields depend on stellar parameters such as mass, age, rotation and accretion rates. Ultimately, such investigations can guide us towards more realistic models of forming Suns, taking into account the effect of magnetic fields in particular.

Magnetic Protostars and Planets (MaPP) is an international project focussing specifically on this issue. It has been granted 690 hr of observing time over 9 consecutive semesters (2008b to 2012b) with the ESPaDOnS spectropolarimeter on the 3.8-m Canada-France-Hawaii Telescope (CFHT) to survey 15 cTTSs and 3 protostellar accretion discs of FU Ori type (FUOrs); it also regularly benefits from contemporaneous observations with the NARVAL spectropolarimeter on the 2-m Télescope Bernard Lyot (TBL) as well as photometric observations from Crimea, Uzbekistan and Armenia. Additional multiwavelength observations from space and/or from the ground are also organised in conjunction with MaPP campaigns on a few specific targets, providing deeper insights into the physical processes under scrutiny (and in particular magnetospheric accretion).

Following a first MaPP paper concentrating on the prototypical low-mass cTTS AA Tau and suggesting that its large-scale magnetic field is strong enough to expel outwards (e.g., through a conical wind) most of the accreted disc material (the propeller regime) and thus to spin-down the protostar efficiently (Donati et al. 2010b), we present a new study revisiting the properties of the large-scale magnetic field of V2129 Oph (after the initial investigation of Donati et al. 2007); in addition to being based on a much better and longer spectropolarimetric data set, this study

also benefits from additional contemporaneous multiwavelength observations from both space (at X-ray frequencies with Chandra/HETGS) and from the ground (high-resolution spectroscopy from HARPS@ESO, low resolution spectroscopy and photometry from the SMARTS facility). A brief overview of the goals of the multiwavelength observing program is given in Gregory et al. (2009).

The present paper concentrates mostly on the spectropolarimetric data, while the other related data sets (and in particular the Chandra/HETGS spectra, Argiroffi et al. in preparation) will be described and analysed in forthcoming companion papers. After briefly recalling the stellar parameters of V2129 Oph, (see Sec. 2), we describe the observed variations of photospheric lines and accretion proxies (Sec. 4) and detail their subsequent modelling with our magnetic imaging code (Sec. 5); we also include a complete remodelling of our older data to ease the comparison of the magnetic images at both epochs. We finally discuss the implications of these new results for our understanding of magnetospheric accretion processes in cTTSs (Sec. 6).

2 V2129 OPH = SR 9 = ROX 29

V2129 Oph is the brightest cTTS in the ρ Oph star formation cloud, with limited visual extinction ($\simeq 0.6$) and a photospheric temperature of $\simeq 4500$ K (spectral type K5, Donati et al. 2007). It exhibits strong H α emission typical to cTTSs (e.g., Bouvier & Appenzeller 1992) and clear infrared excesses and 10 μm silicate emission line fluxes typical of dusty accretion discs (e.g., Furlan et al. 2009) suggesting a disc mass of $\simeq 1 M_\oplus$ (Cieza et al. 2010).

The distance to ρ Oph has recently been redetermined with improved accuracy using VLBA, and estimated to 120 ± 5 pc (Loinard et al. 2008). From the observed maximum visual brightness of V2129 Oph ($m_V \simeq 11.2$, Grankin et al. 2008), the estimated unspotted visual magnitude (11.0 ± 0.2 , Donati et al. 2007) and the visual bolometric correction adequate to V2129 Oph ($\simeq -1.2$, Bessell et al. 1998), one can derive a logarithmic luminosity (with respect to the Sun) of 0.15 ± 0.1 and thus a radius of $R_* = 2.0 \pm 0.3 R_\odot$. This is slightly smaller than that derived in the previous study, directly reflecting the shorter distance to ρ Oph used here.

The rotation period of V2129 Oph estimated from regular photometric variations is found to be 6.53 d in average, varying from about 6.35 to 6.60 d depending on the observing season (Grankin et al. 2008); when compared to other similar stars of the same sample (e.g., V410 Tau, exhibiting no such behaviour), we conclude that this period fluctuation is real. It suggests that differential rotation is shearing the spotted photosphere, producing the observed period fluctuations as starspots migrate in latitude on long timescales – a suggestion that we independently confirm in our study (see Sec. 5). From the rotational broadening of line profiles, the line-of-sight projected equatorial rotation velocity of V2129 Oph is found to be $v \sin i = 14.5 \pm 0.3 \text{ km s}^{-1}$ (Donati et al. 2007), where i is the inclination of the rotation axis to the line of sight. It implies that $R_* \sin i \simeq 1.8 R_\odot$, assuming that the rotation period at the equator is close to the lowest observed periods (i.e., that the photospheric shear of V2129 Oph is Sun-like, with an equator rotating

faster than the poles, as in most other low-mass stars showing differential rotation).

Coupling with the above radius estimate, it suggests that $i \simeq 65^\circ$, with potential values ranging from 50° to 90° . Tomographic imaging (including this study) suggests a smaller inclination angle of $i \simeq 45 \pm 15^\circ$ (Donati et al. 2007). We therefore use an intermediate value, $i \simeq 60^\circ$, slightly larger than in the previous study as a result of the shorter distance assumed for ρ Oph. The corresponding value of the stellar radius is $R_\star \simeq 2.1 R_\odot$ which, when coupled to the temperature, yields a mass of $M_\star \simeq 1.35 M_\odot$ and an age of about $2 - 3$ Myr (Siess et al. 2000); models suggest in addition that V2129 Oph is no longer fully convective and hosts a core whose fractional mass and radius are about one third those of the star. In this context, the corotation radius (at which the Keplerian period is equal to the rotation period of the star) is equal to $r_{\text{cor}} \simeq 7.7 R_\star$ or 0.076 AU.

Mass accretion on V2129 Oph is only moderate. From the equivalent widths and the corresponding line fluxes of the emission lines usually considered as accretion proxies (and in particular the He I D_3 line and the Ca II infrared triplet, IRT) and using the published empirical correlations between lines and accretion fluxes (Fang et al. 2009), we can derive an estimate of the average logarithmic mass accretion rate (in $M_\odot \text{ yr}^{-1}$) at the surface of V2129 Oph, that we find to be equal to -9.2 ± 0.3^1 . Our data also suggest that the mass accretion rate of V2129 Oph is more stable on the long-term (see Sec. 4) than that of cTTSs like AA Tau (showing dominant intrinsic variability on short timescales, Donati et al. 2010b); this preliminary conclusion however needs to be confirmed with longer data sets, to check in particular that we did not catch V2129 Oph in an unusually quiet state of accretion. Optical veiling, i.e., the apparent weakening of the photospheric spectrum (presumably caused by accretion) is apparently weak for V2129 Oph and does not exceed a few %.

3 OBSERVATIONS

Spectropolarimetric observations of V2129 Oph were collected from 2009 July 01 to July 14 using ESPaDOnS on the CFHT. ESPaDOnS collects stellar spectra spanning the whole optical domain (from 370 to 1,000 nm) at a resolving power of 65,000 (i.e., 4.6 km s^{-1}) and with a spectral sampling of 2.6 km s^{-1} , in either circular or linear polarisation (Donati 2003). A total of 23 circular polarisation spectra were collected, at a rate of 2 spectra per night during the first 10 nights. All polarisation spectra consist of 4 individual subexposures lasting each 690 s and taken in different polarimeter configurations to allow the removal of all spurious polarisation signatures at first order.

All raw frames are processed with LIBRE ESPRIT,

¹ Note that this new estimate is an order of magnitude smaller than that mentioned in our previous study (Donati et al. 2007), at the time simply derived by averaging measurements obtained with different methods and thus likely far less accurate; in particular, our new mass accretion rate, computed in exactly the same way as those of V2247 Oph (Donati et al. 2010a) and AA Tau (Donati et al. 2010b), is at least much more consistent with our latter MaPP studies.

Table 1. Journal of observations collected in 2009 July. Columns 1 – 4 respectively list the UT date, the heliocentric Julian date and UT time (both at mid-exposure), and the peak signal to noise ratio (per 2.6 km s^{-1} velocity bin) of each observation (i.e., each sequence of 4×690 s subexposures). Column 5 lists the rms noise level (relative to the unpolarized continuum level I_c and per 1.8 km s^{-1} velocity bin) in the circular polarization profile produced by Least-Squares Deconvolution (LSD), while column 6 indicates the rotational cycle associated with each exposure (using the ephemeris given by Eq. 1).

Date	HJD (2,455,000+)	UT (h:m:s)	S/N	σ_{LSD} ($10^{-4} I_c$)	Cycle (225+)
Jul 01	13.76862	06:21:07	180	2.5	0.692
Jul 01	13.90207	09:33:18	180	2.8	0.712
Jul 02	14.77090	06:24:30	200	2.2	0.845
Jul 02	14.90375	09:35:50	200	2.2	0.866
Jul 03	15.76152	06:11:05	190	2.3	0.997
Jul 03	15.89192	09:18:52	210	1.9	1.017
Jul 04	16.75643	06:03:51	200	2.1	1.150
Jul 04	16.88363	09:07:02	210	1.9	1.169
Jul 05	17.75614	06:03:32	190	2.3	1.303
Jul 05	17.88444	09:08:18	210	2.0	1.322
Jul 06	18.75731	06:05:19	100	4.4	1.456
Jul 06	18.88404	09:07:49	190	2.2	1.475
Jul 07	19.75701	06:04:59	120	4.2	1.609
Jul 07	19.88577	09:10:24	160	3.1	1.629
Jul 08	20.75692	06:04:57	170	2.6	1.762
Jul 08	20.88477	09:09:04	140	3.4	1.782
Jul 09	21.75541	06:02:52	150	3.0	1.915
Jul 09	21.88237	09:05:42	160	2.7	1.935
Jul 10	22.75503	06:02:26	170	2.4	2.068
Jul 10	22.88263	09:06:11	180	2.3	2.088
Jul 12	24.78050	06:39:19	150	3.0	2.378
Jul 13	25.84672	08:14:48	180	2.7	2.542
Jul 14	26.84682	08:15:03	150	3.0	2.695

a fully automatic reduction package/pipeline available at CFHT. It automatically performs optimal extraction of ESPaDOnS unpolarized (Stokes I) and circularly polarized (Stokes V) spectra grossly following the procedure described in Donati et al. (1997). The velocity step corresponding to CCD pixels is about 2.6 km s^{-1} ; however, thanks to the fact that the spectrograph slit is tilted with respect to the CCD lines, spectra corresponding to different CCD columns across each order feature a different pixel sampling. LIBRE ESPRIT uses this opportunity to carry out optimal extraction of each spectrum on a sampling grid denser than the original CCD sampling, with a spectral velocity step set to about 0.7 CCD pixel (i.e. 1.8 km s^{-1}). All spectra are automatically corrected of spectral shifts resulting from instrumental effects (e.g., mechanical flexures, temperature or pressure variations) using telluric lines as a reference. Though not perfect, this procedure provides spectra with a relative radial velocity (RV) precision of better than 0.030 km s^{-1} (e.g., Donati et al. 2008b).

The peak signal-to-noise ratios (S/N, per 2.6 km s^{-1} velocity bin) achieved on the collected spectra (i.e., the sequence of 4 subexposures) range between 100 and 210 depending on weather/seeing conditions, with a median of 180. Rotational cycles E are computed from heliocentric Julian dates according to the ephemeris of Donati et al. (2007):

$$\text{HJD} = 2453540.0 + 6.53E \quad (1)$$

The full journal of observations is presented in Table 1. Observations collected on July 04 (rotation cycles 1.150 and 1.169) were recorded with the (full) moon at an angular distance of only about 2° from V2129 Oph. As a result, the corresponding unpolarized spectra show significant contamination and were discarded from the study; circularly polarised spectra are however unaffected and were kept in the analysis (see Sec. 4 and Fig. 1).

Least-Squares Deconvolution (LSD, Donati et al. 1997) was applied to all observations. The line list we employed for LSD is computed from an ATLAS9 LTE model atmosphere (Kurucz 1993) and corresponds to a K5IV spectral type ($T_{\text{eff}} = 4,500$ K and $\log g = 3.5$) appropriate for V2129 Oph. Only moderate to strong atomic spectral lines (with line-to-continuum core depressions larger than 40% prior to all non-thermal broadening) are included in this list; spectral regions with strong lines mostly formed outside the photosphere (e.g., Balmer, He, Ca II H, K and IRT lines) and/or heavily crowded with telluric lines were discarded. Altogether, about 8,500 spectral features (with about 40% from Fe I) are used in this process. Expressed in units of the unpolarized continuum level I_c , the average noise levels of the resulting Stokes V LSD signatures are ranging from 1.9 to 4.4×10^{-4} per 1.8 km s^{-1} velocity bin.

Almost simultaneous photometry was collected with the SMARTS facility in BVRIJHK bands from rotation cycles 224.3 to 226.9, with a total of 10 to 13 data points depending on the band. These data will be analysed in detail in a forthcoming companion paper; we only use here the V band measurements as a guideline for checking the consistency of our modelling.

4 VARIATIONS OF PHOTOSPHERIC LINES AND ACCRETION PROXIES

As in our previous run (Donati et al. 2007), Zeeman signatures are detected at all times in Stokes V LSD profiles, with peak-to-peak amplitudes varying from 0.2 to 1.0% (see Fig. 1 top right panel). Temporal variations are dominant, the average Stokes V signature being most of the time smaller than the individual ones; moreover, Zeeman signatures are complex and feature several reversals throughout the line profile, suggesting that the parent field topology is not simple. As a result, the line-of-sight projected component of the field averaged over the visible stellar hemisphere and weighted by brightness inhomogeneities (called longitudinal field and estimated from the first moment of the Stokes V profile, e.g., Donati et al. 1997), varying from -360 to $+90$ G, is showing clear non-sinusoidal fluctuations (see Fig. 2 lower left panel) similar to (and about 50% larger than) those observed in 2005 June.

LSD Stokes I profiles of photospheric lines, centred at an average RV of about -7 km s^{-1} , exhibit temporal shape variations, and at times clear asymmetries, (e.g., at rotation cycles 1.303 and 2.542) very reminiscent to those caused by cool spots at the surface of active stars. This is again consistent with the conclusions reached from our first set of observations, where line profiles distortions (smaller than but similar to those reported here) and their evolution with time were successfully interpreted in terms of cool spots at the surface of V2129 Oph (Donati et al. 2007). The observed

photometric variations (see Fig. 2 upper panel) and in particular the corresponding colors (not shown here, to be published in a forthcoming companion paper) also strongly argue that cool spots are present at the surface of the star, with maximum spottedness occurring around phase 0.55, i.e., very close to the phase of strongest photospheric longitudinal field.

We also find that Stokes I LSD profiles show equivalent widths nearly equal to those in the previous data set and roughly constant with time (within $\simeq 2\%$), suggesting that veiling is small. Assuming that the LSD Stokes I profiles with maximum equivalent width correspond to an unveiled spectrum, we derive that veiling is always smaller than 5% (see Fig. 2), except on July 05 where it reaches about 7% as a likely result of a spectral pollution from the nearby full Moon. Comparison with spectral lines of non-accreting TTSs of similar spectral types (e.g., V410 Tau) confirms this conclusion.

We find in particular that LSD Stokes I and V profiles repeat well from one rotation cycle to the next, suggesting that rotational modulation clearly dominates over intrinsic variability. This is particularly clear on the longitudinal field curve (Fig. 2 lower left panel) that repeats almost identically over the 2 successive rotation cycles. In particular, this behaviour is radically different from that of AA Tau where intrinsic variability strongly dominates the photospheric longitudinal field curve (Donati et al. 2010b).

Emission in the He I D_3 line at 587.562 nm , presumably produced in the post-shock region at the footpoints of accretion funnels, is considered as the most reliable accretion proxy. On V2129 Oph, He I emission shows up as a narrow profile and amounts to an average equivalent width of about 11 km s^{-1} (i.e., 0.022 nm), with values ranging from 8 to 19 km s^{-1} (see Fig. 2 and top left panel of Fig. 2). Maximum He I emission is found to occur at phase 0.55, i.e., roughly coincident with times of minimum brightness (i.e., maximum spottedness); it suggests in particular that the accretion region traced by He I emission is close to the cool spot at photospheric level. Centred at an average RV of 0 km s^{-1} , He I emission is significantly red-shifted (by $\simeq 7 \text{ km s}^{-1}$) with respect to LSD photospheric profiles, indicating that it forms in a non-static region above the surface (e.g., the chromosphere) where the post-shock plasma is decelerating towards the star; the line also exhibits sinusoidal RV variations of about $\pm 4 \text{ km s}^{-1}$ about the mean, suggesting that the corresponding emission concentrates in a region centred at phase 0.55 (consistent with the observed maximum He I emission) and presumably at high latitudes (to account for the small amplitude of the observed RV variations). At maximum emission, the emission flux is found to vary by almost a factor of 2 (from 11 to 19 km s^{-1} , i.e., 0.022 to 0.037 nm) between successive rotation cycles (see Fig. 2); the dispersion is smaller at emission minimum (around 9 km s^{-1} , i.e., 0.018 nm). During our previous run, He I emission fluxes were grossly similar, varying from 6 to 19 km s^{-1} (i.e., 0.012 to 0.037 nm) across the rotation cycle.

Clear Zeeman signatures are detected in conjunction with He I D_3 emission (see Fig. 3 top right panel), tracing longitudinal fields ranging from 1.5 to 4.5 kG with magnetic maximum occurring at phase 0.55, i.e., at times of minimum brightness and maximum He I emission (see Fig. 2 second panel left column). As usual for the He I line (e.g.,

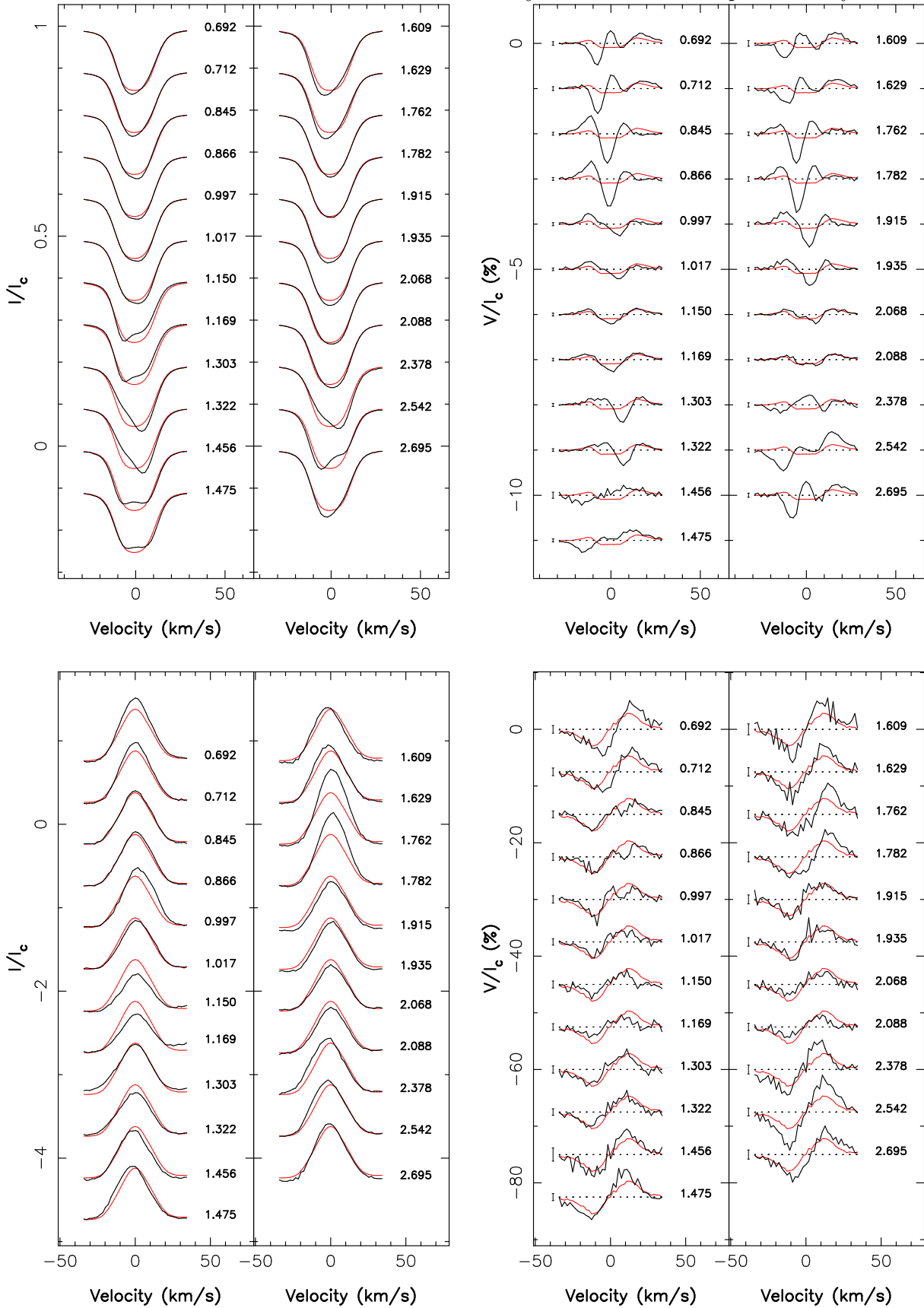


Figure 1. Variation of the Stokes I (left) and Stokes V (right) LSD profiles of the photospheric lines (top) and Ca II IRT lines (bottom) of V2129 Oph in 2009 July. The Stokes I profiles of Ca II emission is shown before subtracting the underlying (much wider) photospheric absorption, hence the reduced flux in the far wings (with respect to the unit continuum). To emphasize variability, the average profile over the run is shown in red. Rotation cycles (as listed in Table 1) and 3σ error bars (for Stokes V data only) are also included next to each profile. Unpolarized profiles recorded on rotation cycles 1.150 and 1.169 are significantly affected by the moon and were discarded from the following study.

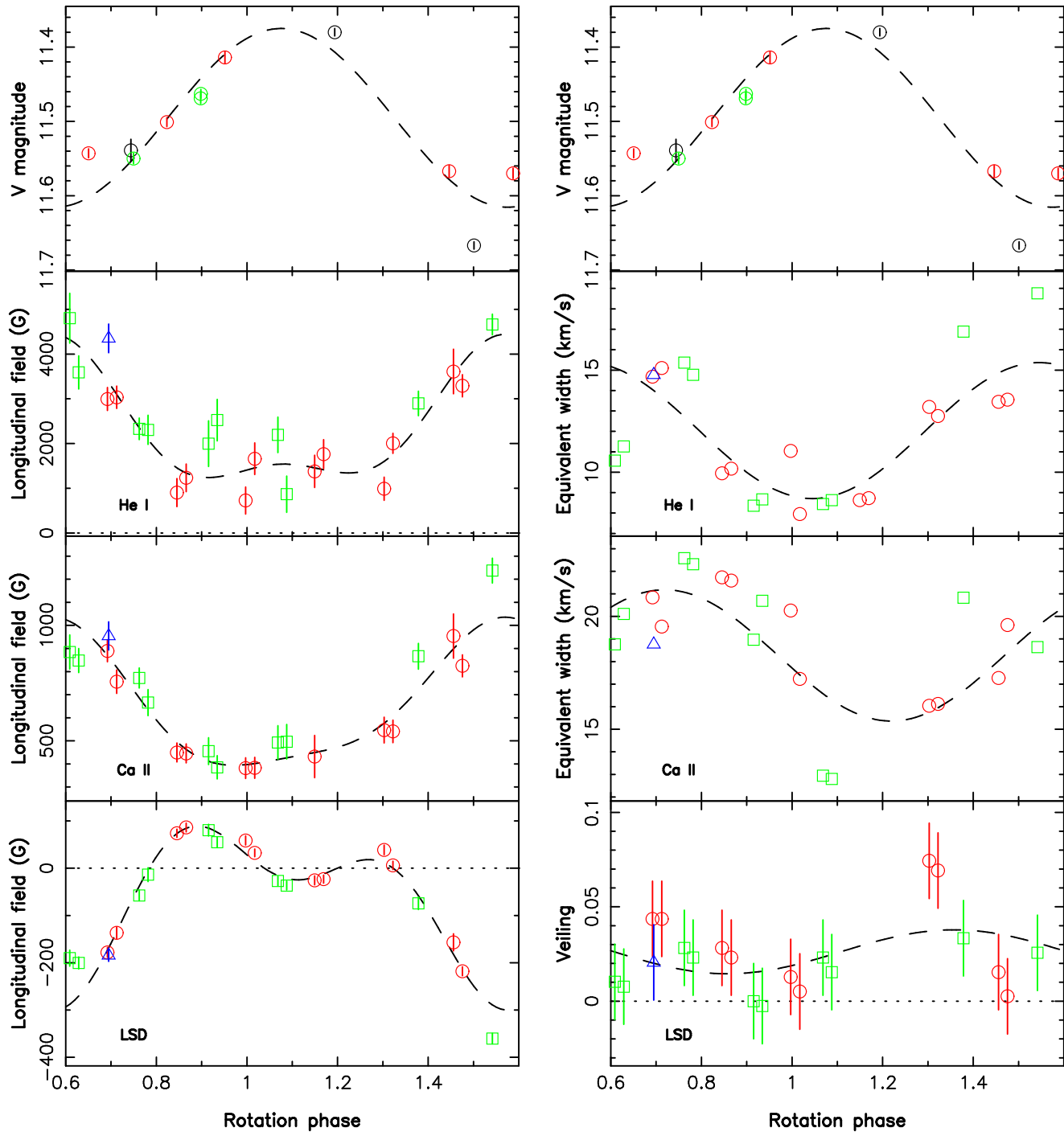


Figure 2. Temporal variations of the integrated brightness (top panels), He I D3 (second panels), Ca II IRT (third panels) and photospheric lines (bottom panels) of V2129 Oph in 2009 July. Longitudinal field variations are shown on the left side (3 lower panels) while equivalent width and veiling variations are shown on the right side. Data collected within cycles 0.6 – 1.6, 1.6 – 2.6 and 2.6 – 3.6 are respectively plotted as red circles, green squares and blue triangles; photometric points shown as black circles were collected one rotation cycle before. Fits with sine/cosine waves (plus first overtones for the left panels) are included (and shown as dashed lines) to outline the amount of variability caused by rotational modulation. $\pm 1 \sigma$ error bars on data points are also shown whenever larger than symbols.

Donati et al. 2007, 2008a), these Zeeman signatures feature a markedly non-antisymmetric shape (with a blue lobe stronger and narrower than the red one) indicating that the line is formed within a region featuring a strong velocity gradient, nicely supporting the idea that it traces non-static, chromospheric post-shock plasma decelerating towards the

surface of the star. Note that longitudinal fields at similar phases but different rotation cycles grossly agree with each other, even when He I emission fluxes (and thus presumably accretion rates) are significantly different (e.g., at cycles 1.609 and 2.542), indirectly confirming that He I emission is probing localised regions with well defined field strengths

and orientations at the surface of the star. These longitudinal field estimates are significantly larger than those estimated in the previous study (Donati et al. 2007), by a typical factor of 2 – 3; it reveals in particular that the large-scale field of V2129 Oph strongly varied on a timescale of only 4 yr. Maximum longitudinal fields from LSD and He I profiles are found to occur at roughly the same phase in the present run, while they were shifted by about 0.25 cycle in our previous data set; this is additional confirmation that the large-scale field topology significantly changed between the two epochs.

Core emission in Ca II IRT lines is another very useful probe of magnetospheric accretion, even though it often features a significant contribution from non-accreting chromospheres and is thus a more ambiguous proxy than He I emission. However, the redder spectral location, the higher magnetic sensitivity and the multiple nature of the corresponding spectral lines more than compensate for this drawback; with their classical, nearly-antisymmetric profiles (with respect to the line center, see Fig. 1 bottom right panel), the Zeeman signatures of Ca II IRT lines are also simpler and easier to model than those of the He I line. To extract the core Ca II emission profiles (used later in the imaging analysis, see Sec. 5) from our spectra, we start by constructing a LSD-like weighted average of the 3 IRT lines; we then subtract the underlying (much wider) photospheric absorption profile, with a Lorentzian fit to the far wings over a velocity interval of $\pm 200 \text{ km s}^{-1}$ about the emission core. IRT emission is centred at a RV of about -6 km s^{-1} , i.e., redshifted by only 1 km s^{-1} with respect to LSD photospheric lines (as opposed to 7 km s^{-1} for the He I line), confirming that it traces slowly-moving regions of the post-shock accretion funnels that are closer to the surface of the star. In 2009 July, equivalent widths of the Ca II emission are in average equal to about 18 km s^{-1} (i.e., 0.050 nm) and vary from 12 to 24 km s^{-1} (i.e., 0.035 – 0.070 nm) as a result of both rotational modulation and intrinsic variability (see Fig. 2 right column third panel); maximum IRT emission is found to occur at phase 0.70, i.e., 0.15 rotation cycle later than He I emission and magnetic maxima. RVs of IRT emission are found to vary by about $\pm 2 \text{ km s}^{-1}$ about the mean, consistent with a localised emission region centred at phase 0.70 and at high latitudes.

Clear Zeeman signatures are detected at all epochs in conjunction with Ca II IRT emission, featuring peak-to-peak amplitudes of up to about 10% (see Fig. 1 bottom right panel). Corresponding longitudinal fields vary from 0.4 to 1.2 kG (see Fig. 2 left column third panel); this is about twice larger than in our previous data set (Donati et al. 2007), confirming again that the field has considerably strengthened within the corresponding 4 yr. Maximum longitudinal field is observed at phase 0.55, i.e., in conjunction with the magnetic maximum traced by He I lines. The longitudinal field curve is found to repeat fairly well over the two rotation cycles, clearly demonstrating that rotational modulation is dominant. The ratio of He I to Ca II longitudinal fields is $\simeq 4$ across the whole run; this essentially reflects that Ca II longitudinal fields suffer from dilution and flux cancellation (with respect to those from He I) as a result of Ca II emission forming over a much wider area (including in particular the quiet chromosphere) while He I emission traces only the accretion regions.

As usual for cTTSs, Balmer lines (and in particular H α and H β) are in emission and show clear temporal variability and rotational modulation (see Fig. 3 lower panel). As in our previous data set, H α and H β mostly show one main emission peak centred at about -15 km s^{-1} , blue-shifted by about 8 km s^{-1} with respect to the LSD photospheric profiles; the average equivalent widths of both profiles are equal to 800 and 150 km s^{-1} respectively (i.e., 1.7 and 0.24 nm), i.e., very similar to those measured in 2005 June. Looking at the variance profiles of both lines (see Fig. 4), one can see that temporal variations mostly affect the central emission peak and the red wing, both parts of the line being anti-correlated with each other; this is similar to what was reported from our previous data set, except that variations in the central peak are now smaller than in 2005 June while those in the red wing are both larger and shifted to smaller velocities (with the variance profile now peaking at 100 km s^{-1} instead of 150 km s^{-1}). In our new data set, Balmer emission and profile variations are also clearly visible in the blue wing (around -170 km s^{-1}), both in H α and H β (see Fig. 4); this emission component was not detected in the previous data set.

Recurrent absorption episodes in the red wing of Balmer lines are usually interpreted as evidence for accretion veils anchored in the inner regions of the surrounding disc and periodically intersecting the line of sight as the star rotates (e.g., Bouvier et al. 2007). Those observed on V2129 Oph in 2009 July occur between phases 0.6 and 0.9 (see Fig. 3 lower panel), i.e., 0.05 – 0.35 rotation cycle (or 0.20 cycle in average) after He I and magnetic maxima; it suggests that the corresponding accretion veils are trailing the main magnetic spot detected at the surface of the protostar (centred at phase 0.55). In 2005 June, these absorption episodes were shorter, being visible for less than 15% of a rotation cycle and occurring slightly (about 0.05 rotation cycle) before magnetic maximum (Donati et al. 2007).

From the average equivalents widths of the He I, Ca II IRT, H β and H α lines, we derive logarithmic line fluxes (with respect to the luminosity of the Sun L_{\odot}) equal to -5.1 , -4.8 , -4.1 and -3.2 respectively², implying logarithmic accretion luminosities (with respect to L_{\odot}) of -2.0 , -2.0 , -2.3 and -1.7 respectively (using empirical correlations from Fang et al. 2009). As estimates from the two main accretion proxies agree with each other and with the overall mean, we can safely conclude that the average logarithmic accretion luminosity of V2129 Oph is -2.0 ± 0.3 and thus that the average logarithmic mass accretion rate (in $M_{\odot} \text{ yr}^{-1}$) is equal to -9.2 ± 0.3 . Using the same relations, we find that the logarithmic accretion rate at magnetic maximum is typically -9.0 (with peaks of up to -8.9) and about -9.4 around magnetic minimum (i.e., phase 0.05), the observed fluctuation most likely tracing the varying viewing configuration (rather than an intrinsic change in the accretion rate). Mass accretion rates can independently be estimated through the full width of H α at 10% height (e.g., Natta et al.

² To derive line fluxes from normalized equivalent widths, we approximate the continuum level by a Planck function at the temperature of the stellar photosphere. Results are found to be compatible with those in the published literature (e.g., Mohanty et al. 2005) within better than 0.1 dex.

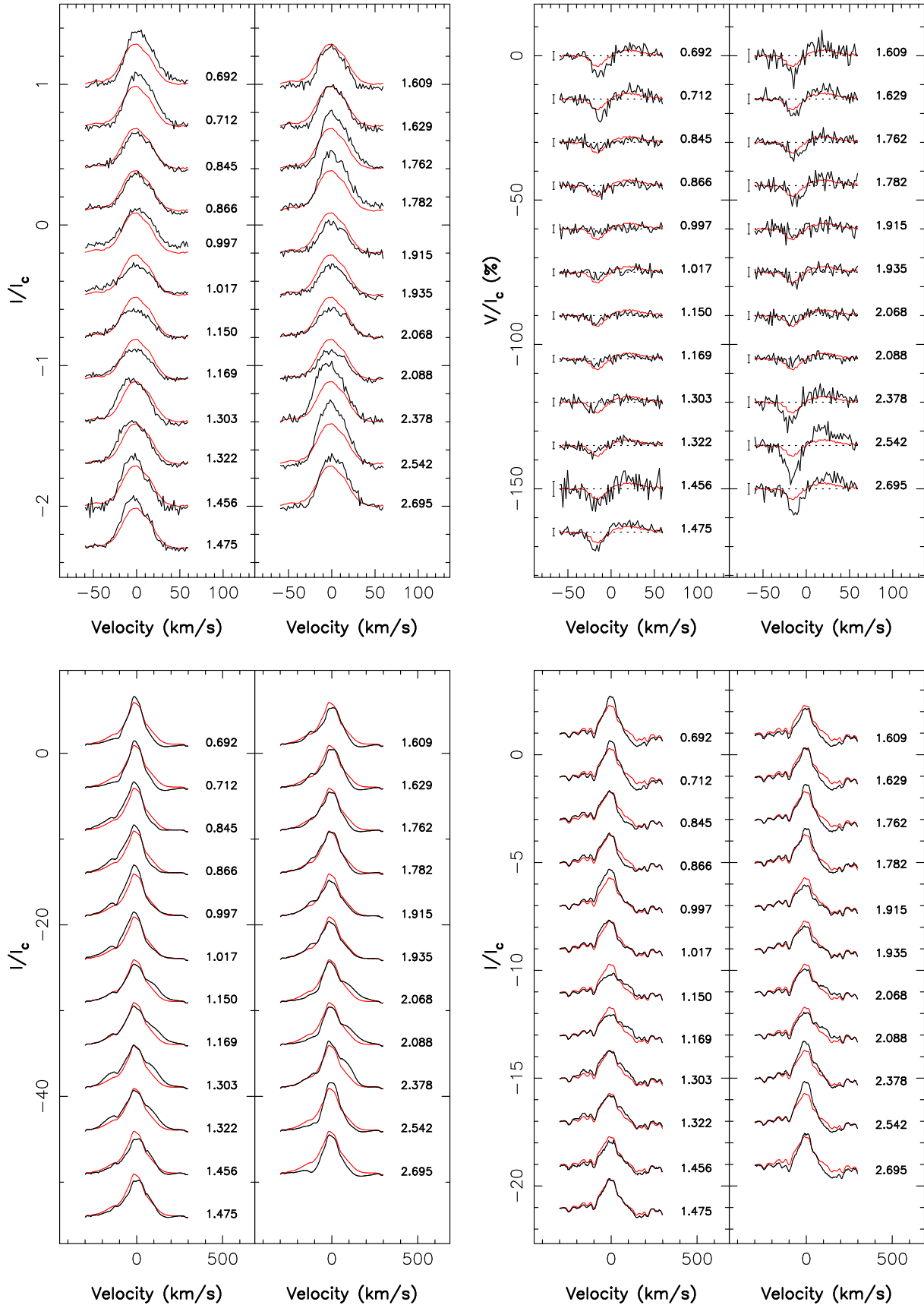


Figure 3. Variation of the He I D_3 (Stokes I : top left, Stokes V : top right), $H\alpha$ (bottom left) and $H\beta$ (bottom right) lines of V2129 Oph in 2009 July. To emphasize variability, the average profile over the run is shown in red. Rotation cycles (as listed in Table 1) and 3σ error bars (for Stokes V data only) are also mentioned next to each profile.

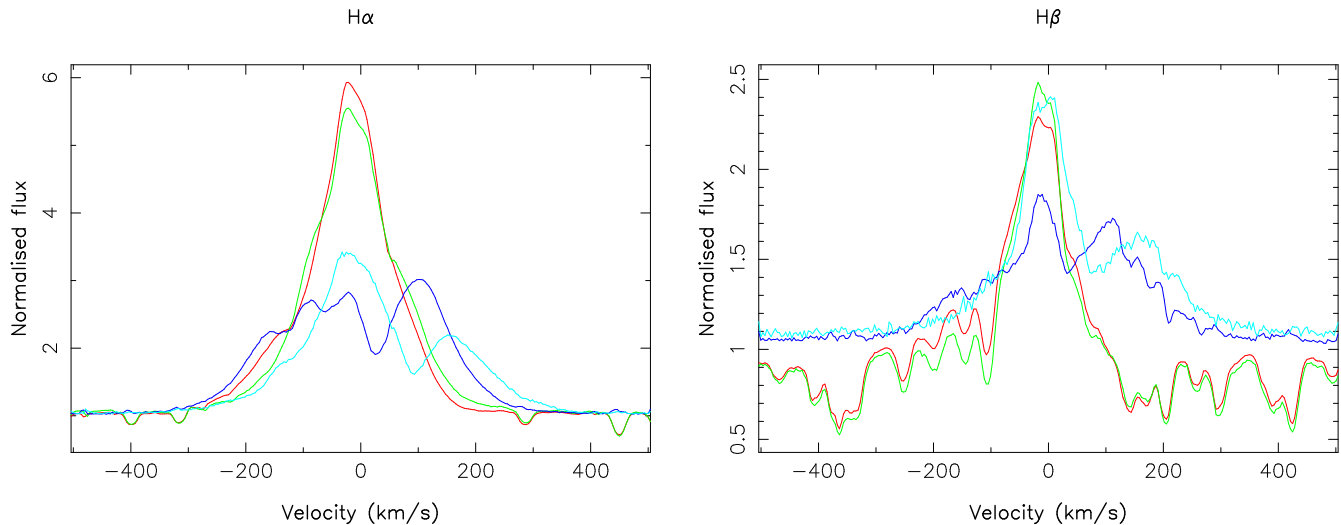


Figure 4. Average (2009 July: red, 2005 June: green) and standard deviation (2009 July: dark blue, 2005 June: light blue) profiles of H α (left panel) and H β (right panel) of V2129 Oph at both observing epochs. Standard deviation profiles are expanded by a factor of 3 and shifted upwards by 1 for graphics purposes.

2004; Cieza et al. 2010); in the case of V2129 Oph in 2009 July, H α exhibits a full width of 350 km s^{-1} implying an logarithmic mass accretion rate estimate of -9.4 ± 0.6 in reasonably good agreement with our main estimate.

Line equivalent widths and fluxes measured during our 2005 run (and in particular those of He I and Ca II IRT accretion proxies) are basically identical to those listed here, suggesting that the mass accretion rate at the surface of V2129 Oph is roughly stable (within a factor of $\simeq 2$) on long timescales as well; in particular, this is different than the behaviour reported for AA Tau, where the mass accretion rate can vary by an order of magnitude between successive rotation cycles (Donati et al. 2010b). Further data collected over a longer time span are however needed to confirm that we did not catch V2129 Oph in an unusually quiet state of accretion at both epochs.

5 MODELLING THE SURFACE OF V2129 OPH

5.1 Overview of the modelling method

Using the set of LSD and Ca II IRT profiles of V2129 Oph described in the previous section, we can recover the large-scale field topology at the surface of the protostar, as well as maps of how photospheric brightness and accretion-powered Ca II emission distributes with longitude and latitude. In this aim, we apply our new modelling technique, detailed extensively and proved successful in a previous MaPP study (Donati et al. 2010b). In the present paper, we only briefly describe the technical aspects of this method and concentrate on its specific application to our new V2129 Oph data set; we also carry out a new analysis of the older data set (collected in 2005 June and analysed with an experimental version of our imaging tool, Donati et al. 2007) to allow a more direct and meaningful comparison of reconstructed maps.

Following the principles of maximum entropy, our code automatically derives the simplest magnetic topology, photospheric brightness image and accretion-powered Ca II

emission map compatible with the series of rotationally modulated Stokes I and V LSD and Ca II IRT profiles. The reconstruction process is iterative and proceeds by comparing at each step the synthetic Stokes I and V profiles corresponding to the current images with those of the observed data set. The magnetic field is described through its poloidal and toroidal components expressed as spherical-harmonics (SH) expansions (Donati et al. 2006). The spatial distribution of photospheric brightness (with respect to the quiet photosphere) and that of accretion-powered Ca II emission (in excess of and with respect to that produced by the quiet chromosphere) are modelled as series of independent pixels (typically a few thousand) on a grid covering the visible surface of the star (with spots in the brightness image assumed to be darker/cooler than the quiet photosphere and spots in the accretion-powered Ca II emission map supposed to be brighter than the quiet chromosphere).

Synthetic profiles are computed by summing up the elementary spectral contributions from each image pixel over the visible hemisphere, taking into account all relevant local parameters of the corresponding grid cell (e.g., brightness, accretion-powered excess emission, magnetic field strength and orientation, radial velocity, limb angle, projected area). Since the problem is partly ill-posed, we stabilise the inversion process by using an entropy criterion (applied to the SH coefficients and to the brightness/excess emission image pixels) aimed at selecting the field topologies and images with minimum information among all those compatible with the data. The relative weights attributed to the various SH modes can be imposed, e.g., for purposely producing antisymmetric or symmetric field topologies with respect to the centre of the star (by favouring odd or even SH modes, Donati et al. 2007, 2008a). More details concerning the specific description of local profiles used in the model can be found in Donati et al. (2010b).

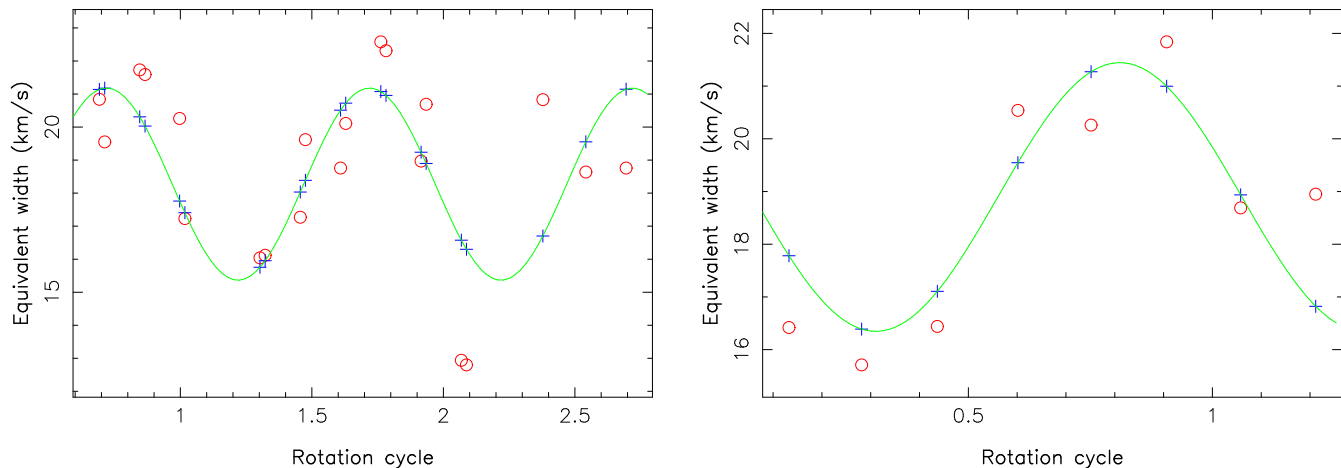


Figure 5. Measured (red open circles) and fitted (blue pluses) equivalent widths of the Ca II IRT LSD profiles of V2129 Oph in 2009 July (left panel) and 2005 June (right panel). The model wave (green line) providing the best (sine+cosine) fit to the data (with a period of 6.53 d) presumably traces rotational modulation, while the deviation from the fit illustrates the strength of intrinsic variability.

5.2 Application to V2129 Oph

Our imaging model assumes that the observed profile variations are mainly due to rotational modulation, and potentially to surface differential rotation as well when the star is observed for at least several rotation cycles; all other sources of profile variability (and in particular intrinsic variability) cannot be properly reproduced and thus contribute as noise into the modelling process, degrading the imaging performance and potentially even drowning all relevant information. Filtering out significant intrinsic variability from the observed profiles is thus worthwhile to optimise the behaviour and convergence of the imaging code.

We implement this by applying specific corrections on our data set. We first suppress veiling by scaling all LSD Stokes I and V photospheric profiles, to ensure that unpolarized lines have the same equivalent widths. We also remove the non rotationally-modulated part in the observed fluctuations of Ca II IRT emission, by fitting them with a sine+cosine wave (see Fig. 5) and by scaling the corresponding Stokes I and V profiles accordingly, thus ensuring that equivalent widths of unpolarized lines match the optimal fit. Although only approximate (especially the removal of the intrinsic variability), this procedure is at least very straightforward and has proved successful when applied to real data (e.g., Donati et al. 2010b) and efficient at retaining rotational modulation mostly.

The reconstructed magnetic, brightness and accretion maps of V2129 Oph are shown in Fig. 6, with corresponding fits to the data shown in Figs. 7 and 8; we also include new maps (and fits) derived from the previous data set, but reconstructed with our new modelling method to ease comparison between the two sets of images. The SH expansion describing the field was limited to terms with $\ell \leq 8$, very small power being reconstructed in higher order modes. Both images were reconstructed assuming that the field is antisymmetric with respect to the centre of the star (see below).

The overall fits to the data are reasonably good, reproducing the data down to reduced chi-squares χ_r^2 of about 2 (starting from initial χ_r^2 of 25 and 40 for the 2009 July and 2005 June data sets respectively). Optimal fits are obtained

for $v \sin i = 14.5 \pm 0.5 \text{ km s}^{-1}$ and $v_{\text{rad}} = -7.0 \pm 0.1 \text{ km s}^{-1}$; Ca II IRT lines are found to be slightly redshifted (by about 1 km s^{-1}) with respect to photospheric lines, as usual for cTTSs. We also find that optimal fits to the observed Stokes V profiles can be achieved when setting the local filling factor ψ , describing the relative proportion of magnetic areas at any given point of the stellar surface, to $\psi \simeq 0.4 \pm 0.1$. The emission profile scaling factor ϵ , describing the emission enhancement of accretion regions over the quiet chromosphere, is again set to $\epsilon = 10$ (as in Donati et al. 2010b), yielding fractional areas of accretion spots of about 2–3% at both epochs. Most other model parameters, and in particular those describing the local line profiles, are either identical or very similar to those chosen in our previous studies; for more information, the reader is referred to Donati et al. (2010b).

5.3 Results

The reconstructed large-scale magnetic topology of V2129 Oph in 2009 July is mostly poloidal, with only 5% of the magnetic energy in the toroidal component; this poloidal component is mainly antisymmetric, with at least $\simeq 60\%$ of the energy concentrating in modes with $m < \ell/2$. We find that the field is more likely to be antisymmetric about the centre of the star, a symmetric topology requiring much more magnetic energy to produce the same fit to the data. The dominant terms in the reconstructed SH expansion of the large-scale poloidal field correspond to $\ell = 3$ (with $m = 0, 1$, i.e., a moderately tilted octupole) and $\ell = 1$ (with $m = 0$, i.e., an aligned dipole), whose respective intensity at the pole are about $2.1 \pm 0.3 \text{ kG}$ and $0.9 \pm 0.1 \text{ kG}$ respectively; from different reconstructions with slightly different input parameters and reconstruction schemes, we estimate that the octupole is typically 2–3 stronger than the dipole. The main magnetic feature that we reconstruct is a high-latitude radial field region where the magnetic intensity peaks at about 4 kG, slightly smaller though comparable to the maximum fields traced by the He I line (about 5 kG, see Fig. 2); this main magnetic region is centred at phase 0.5, compatible with the estimate guessed in Sec. 4 from the longitudinal

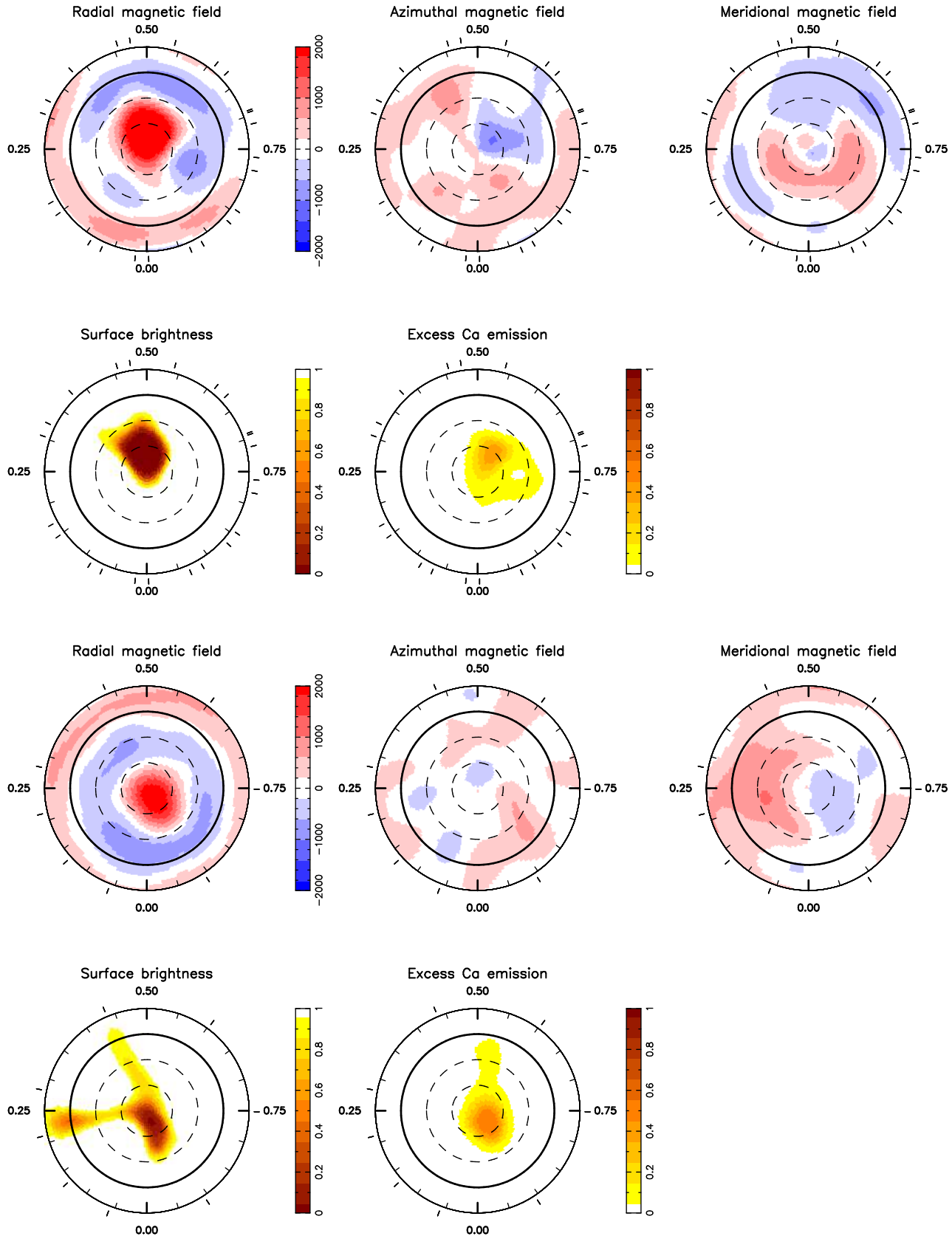


Figure 6. Maps of the radial, azimuthal and meridional components of the magnetic field \mathbf{B} (first and third rows, left to right panels respectively), photospheric brightness and excess Ca II IRT emission (second and fourth rows, first and second panels respectively) at the surface of V2129 Oph in 2009 July (two upper rows) and 2005 June (two lower rows). Magnetic fluxes are labelled in G; local photospheric brightness (normalized to that of the quiet photosphere) varies from 1 (no spot) to 0 (no light); local excess Ca II emission varies from 0 (no excess emission) to 1 (excess emission covering 100% of the local grid cell, assuming an intrinsic excess emission of $10\times$ the quiet chromospheric emission). In all panels, the star is shown in flattened polar projection down to latitudes of -30° , with the

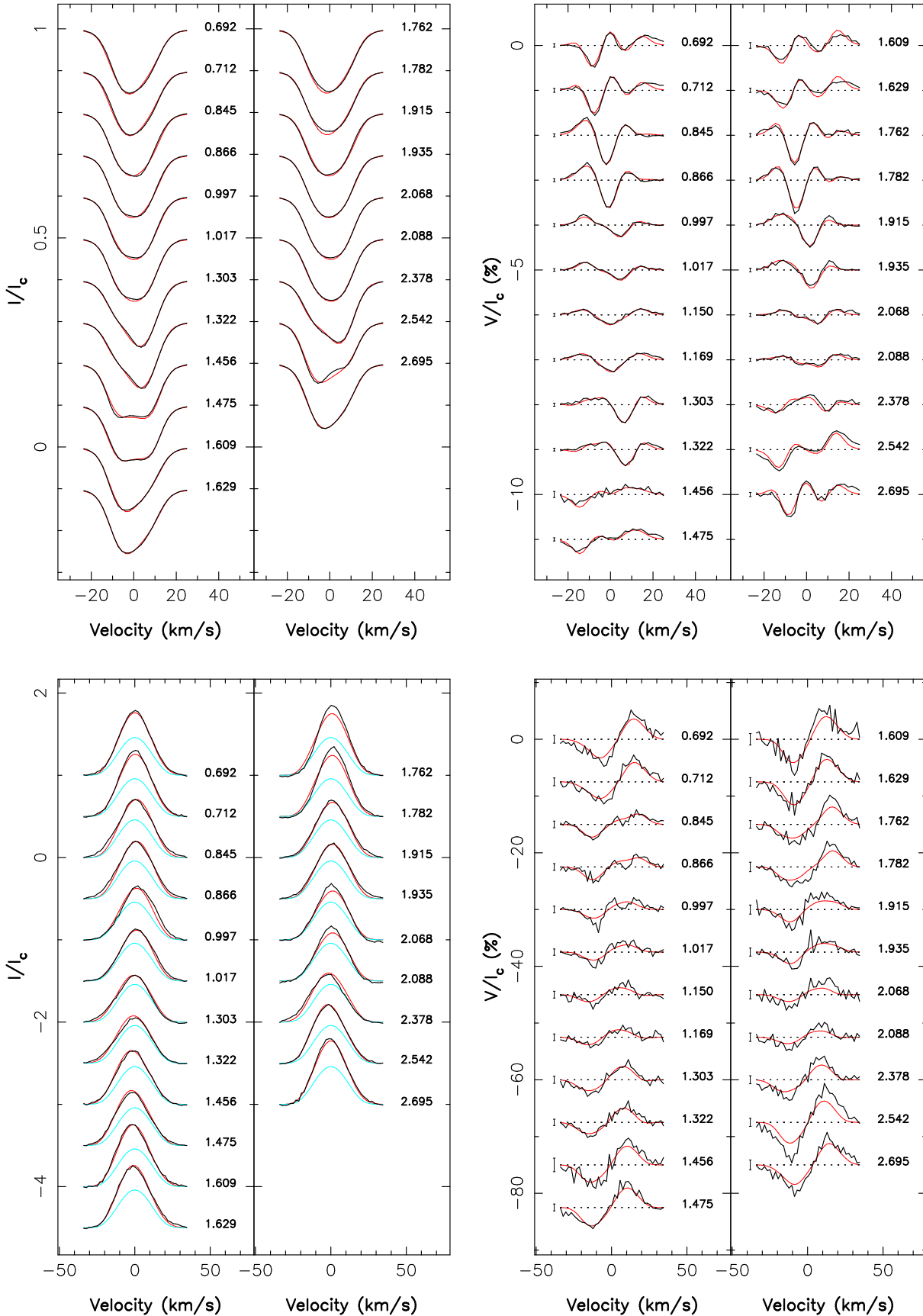


Figure 7. Maximum-entropy fit (thin red line) to the observed (thick black line) Stokes I and Stokes V LSD photospheric profiles (first two panels) and Ca II IRT profiles (last two panels) of V2129 Oph in 2009 July. The light-blue curve in the bottom left panel shows the (constant) contribution of the quiet chromosphere to the Stokes I Ca II profiles. Rotation cycles and 3σ error bars (for Stokes V profiles) are also shown next to each profile.

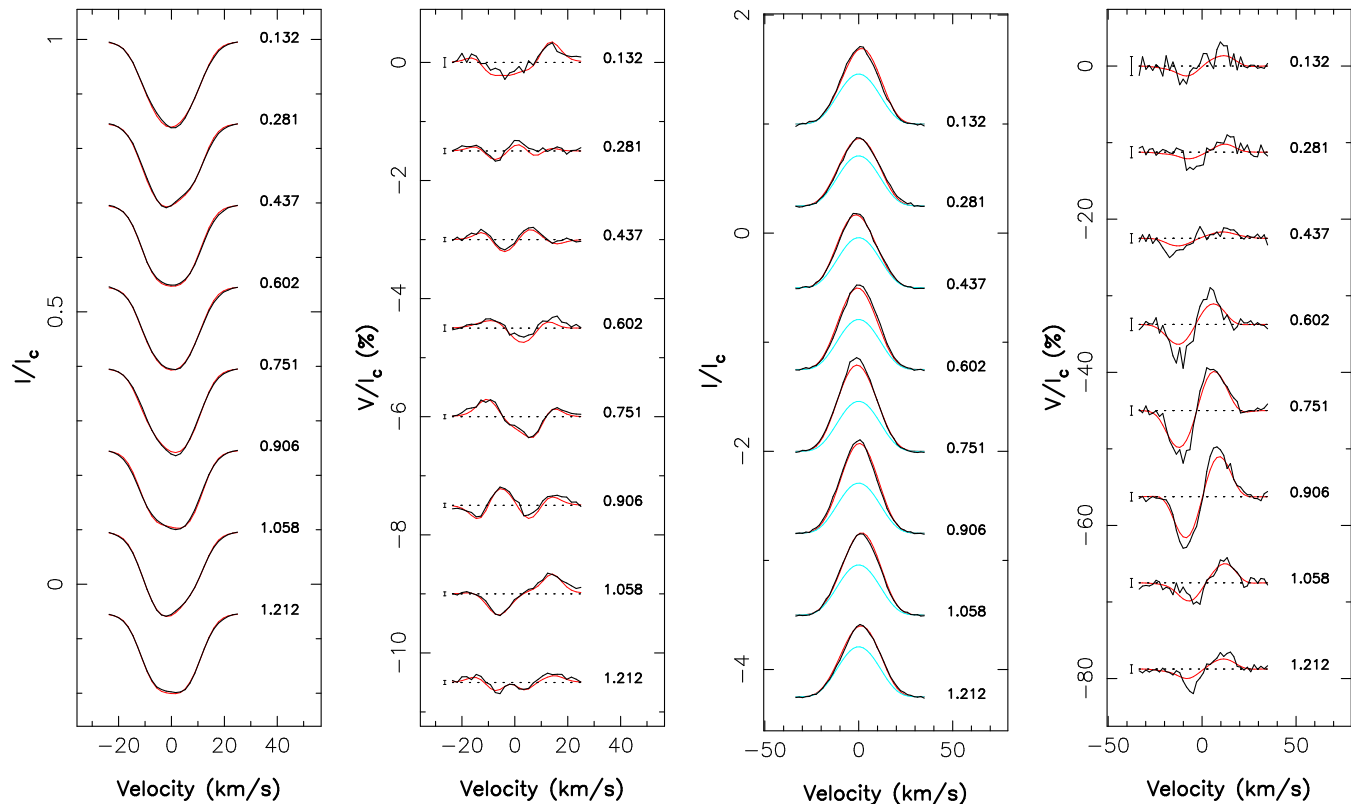


Figure 8. Same as Fig. 7 for the 2005 June data set.

field curves of both Ca II IRT and He I lines. The octupole component of the poloidal field can be directly traced in the reconstructed magnetic map, as a low-latitude ring of negative radial field encircling the main high-latitude radial field region.

The reconstructed magnetic maps of V2129 Oph in 2005 June are grossly similar to those of 2009 July except for the large change in the overall field intensity; they are also compatible with the preliminary version of Donati et al. (2007). Again, the large-scale field is found to be mostly poloidal and axisymmetric, with the poloidal component being dominated by a moderately tilted octupole (with a polar strength of about 1.5 ± 0.3 kG); the dipole component is typically 5 times smaller than the octupole component, with polar strengths of about 0.3 kG. The high-latitude radial field region features peak intensities of about 2 kG, slightly larger though compatible with fields traced by the He I line. The phase at which this high field region is located is different in 2009 July and 2005 June; however, this difference likely reflects no more than the uncertainty on the rotation period. The reconstructed maps thus confirm the preliminary conclusions of Sec. 4 about the overall strengthening of the field (by typically a factor of 2) between 2005 and 2009; they further suggest that this increase mostly concerns the dipole component of the field (about thrice stronger in 2009) and to a lesser extent its octupole component (about 50% stronger in 2009).

The photospheric brightness map we reconstruct for V2129 Oph in 2009 July essentially features one large dark spot at high latitude covering about 6.5% of the total stellar surface (i.e., about 25% of the visible hemisphere at maxi-

mum visibility) and within most of which the brightness contrast at visible wavelengths (with respect to the surrounding photosphere) is larger than 20; this dark spot mostly overlaps the strongly magnetic region discussed above, making the latter hardly visible at optical wavelengths (hence its non-detection in LSD profiles and in the corresponding longitudinal field curve, see Fig. 2). This photospheric brightness map is also grossly consistent (both in phase and amplitude) with the observed photometric light-curve of V2129 Oph, even though the latter was not used in the modelling. The photospheric brightness map corresponding to 2005 June (again compatible with, though less detailed than, the previous version of Donati et al. 2007) features a smaller and less contrasted high-latitude dark spot as well as low-latitude appendages, covering altogether about 5% of the total stellar surface. As in 2009 July, the high-latitude spot is mostly coincident with the strongly magnetic region of the radial field map. We estimate that the increase in size and contrast of the high-latitude dark spot on V2129 Oph between 2005 and 2009 is real, and readily traceable in the comparatively larger distortions (by about a factor of 2 in average, as judged from standard deviation profiles) in the unpolarized LSD profiles of the 2009 data set (see first panels of Figs. 7 and 8).

The map of accretion-powered excess emission that we reconstruct from the 2009 July data set shows one main high-latitude region, covering about 2.5% of the total stellar surface. This region is located at phase 0.6, i.e., slightly trailing by about 0.1 cycle the main radial field region and the dark photospheric spot; this phase shift is readily traceable in the rotational modulation of both the equivalent widths

and radial velocities of the Ca II IRT emission (see Sec. 4), suggesting that it is real even though corresponding to a spatial size comparable to our resolution element at the surface of the star. A similar accretion region is reconstructed from the 2005 June data set, this time overlapping the main field region and dark photospheric spot.

Our modelling can also estimate the amount by which the photosphere is sheared by differential rotation (e.g., Donati et al. 2003, 2010a). This is done by assuming that the rotation rate at the surface of the star is varying with latitude θ (as $\Omega_{\text{eq}} - d\Omega \sin^2 \theta$ where Ω_{eq} is the rotation rate at the equator $d\Omega$ the difference in rotation rate between the equator and the pole), and by determining the pair of differential parameters Ω_{eq} and $d\Omega$ that produces the best fit to the data at a given image information content. Since differential rotation is estimated from subtle departures with respect to pure rotational modulation, we only use LSD photospheric profiles for this task, in order to minimise all other potential sources of intrinsic variability. When using Stokes V profiles, we find a clear minimum in the χ_r^2 map, located at $\Omega_{\text{eq}} = 0.974 \pm 0.005 \text{ rad d}^{-1}$ and $d\Omega = 0.036 \pm 0.015 \text{ rad d}^{-1}$ (see Fig. 9). The corresponding rotation periods for the equator and pole are $6.45 \pm 0.04 \text{ d}$ and $6.70 \pm 0.15 \text{ d}$ respectively, compatible (within $\simeq 2\sigma$) with the range of reported photometric periods (ranging from 6.35 to 6.60 d Grankin et al. 2008). This is also compatible (within $\simeq 2\sigma$) with the preliminary estimate derived from the 2005 Stokes I data set. No clear χ_r^2 minimum is observed when using the LSD Stokes I profiles from 2009 July.

From our new estimate alone, we cannot firmly exclude that V2129 Oph is rotating rigidly; if this were the case, the most likely rotation period (i.e., that minimising χ_r^2) would be $6.52 \pm 0.01 \text{ d}$, close to that assumed here for phasing data (equal to 6.53 d, see Eq. 1). Rigid rotation is however unlikely given the observed variability of the photometric period. At 99% confidence level, we can ascertain that the photospheric shear of V2129 Oph is Sun-like in sign (i.e. with a fast equator and slow pole) and smaller than $\simeq 0.07 \text{ rad d}^{-1}$ (about that of the Sun). The corresponding time for the equator to lap the pole by one complete rotation cycle is found to be $175_{-52}^{+125} \text{ d}$, and is larger than 90 d at 99% confidence level. Images presented in Fig. 6 are reconstructed assuming our new estimate of the photospheric shear; images derived assuming rigid rotation (with a period of 6.53 d) are however virtually identical to those presented here (as expected from the small differential rotation).

6 SUMMARY AND DISCUSSION

This paper presents new results of the MaPP project, focussing on the impact of magnetic fields on star formation, during the cTTS phase in particular. Here we concentrate on V2129 Oph, the brightest cTTS of the ρ Oph star formation cloud, for which we present new spectropolarimetric data collected in 2009 July with ESPaDOnS@CFHT, covering 2 complete rotation cycles of the protostar and augmented from almost simultaneous photometric data collected with SMARTS; additional multiwavelength data (e.g., X-ray data from Chandra/HETGS, visible spectra from HARPS@ESO and SMARTS) were also collected as part of this campaign and will be presented in forthcoming companion papers.

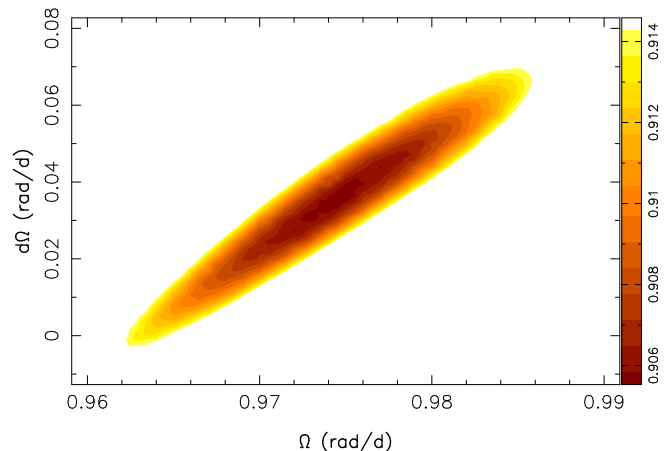


Figure 9. Variation of χ_r^2 as a function of Ω_{eq} and $d\Omega$, derived from the modelling of Stokes V LSD profiles at constant information content. The outer color plot corresponds to a χ_r^2 increase of 1% corresponding to a 99% confidence interval (for each parameter considered separately) given the number of data points adjusted in the process (644).

From these time-resolved data and using the last version of our tomographic techniques, we reconstruct maps of the large-scale magnetic field, of the photospheric brightness and of the accretion-powered Ca II IRT excess emission at the surface of V2129 Oph; we also include in the paper a complete re-analysis of our old spectropolarimetric data collected in 2005 July, to ease comparison with our newest results.

The large-scale field of V2129 Oph is found to be mostly poloidal and axisymmetric, and essentially consists of a $\simeq 2.1 \text{ kG}$ octupole and a $\simeq 0.9 \text{ kG}$ dipole, both tilted by about 20° with respect to the rotation axis; the main magnetic feature reconstructed on the map is a 4 kG high-latitude radial field region. We also find that the large-scale field strongly increased by typically a factor of 2 since 2005 June, with the dipole component enhanced by a factor of $\simeq 3$ and the octupole component by about 50%; in this process, the octupole to dipole intensity ratio has decreased by a factor of $\simeq 2$, from about 5 (in 2005) down to $\simeq 2.5$ (in 2009). This change is readily visible on the main high-latitude radial field feature, whose average magnetic strength (as determined from, e.g., Ca II IRT or He I lines) has increased by at least a factor of 2 between both epochs. We finally report that the surface differential rotation by which the detected large-scale field is sheared is Sun-like in sign (with a fast equator and slow poles) and weaker than solar in strength (by about a factor of 2).

We consider that the change in the large-scale magnetic topology of V2129 Oph is unambiguous evidence that its field is generated by dynamo processes, rather than being a fossil remnant of earlier formation stages; although this conclusion was anticipated both on observational and theoretical grounds (e.g., Donati & Landstreet 2009), its firm demonstration is nevertheless a significant step forward in our understanding of the origin of magnetic fields in low-mass protostars. Our result suggests that dynamo fields of cTTSs are variable on a timescale of a few years and are thus intrinsically non-stationary; a regular magnetic monitoring of a small sample of low-mass protostars should be able to re-

veal whether these dynamos are cyclic, and if so, provide an estimate of the typical period of their magnetic cycles. The recent report that two cTTSs with virtually identical stellar parameters and evolutionary states (namely BP Tau and AA Tau) show discrepant magnetic topologies (with unequal dipole to octupole intensity ratios, respectively equal to $\simeq 1$ and >5 respectively) and different dipole strengths in particular (by about a factor of 2), although intriguing at first sight, seems consistent with what we observe on V2129 Oph (where we see a comparable change in dipole field strength between 2005 and 2009).

Our data also indicate that areas of enhanced accretion-powered Ca II and He I emission are close to the main magnetic region of V2129 Oph, as in all cTTSs monitored with MaPP up to now; it confirms in particular that this strong field region (and its immediate vicinity) is where accretion funnels, linking the protostar to the inner edge of its accretion disc, are anchored. We further demonstrate that in V2129 Oph, these strong magnetic regions are coincident, at photospheric level, with large dark spots featuring a high brightness contrast with the neighbouring photosphere and generating most of the observed photometric variations. We also find that this dark spot is increasing in size and contrast between 2005 and 2009, i.e., when the field in main magnetic region strengthens, in line with theoretical expectations that stronger fields are more efficient at inhibiting local convection. We note that the observed photometric modulation of V2129 Oph cannot be attributed to partial occultations of the protostar by the accretion warp at the inner disc edge like those seen on AA Tau (e.g., Bouvier et al. 2007); these occultations are indeed generating photometric eclipses that are deep (usually larger than 1 mag), color specific (Bouvier et al. 1999) and lagging phases of magnetic maxima (Donati et al. 2010b), at variance with what we report here for V2129 Oph. It confirms at the same time that the rotation axis of V2129 Oph is likely not inclined by more than 60° with respect to the line of sight (see Sec. 2).

Using the He I D_3 , Ca II IRT, $H\beta$ and $H\alpha$ emission fluxes along with the empirical correlations of Fang et al. (2009), we derive that the average logarithmic accretion rate of V2129 Oph (in $M_\odot \text{ yr}^{-1}$) is -9.2 ± 0.3 , peaking at -9.0 in average at magnetic maximum (i.e., phase 0.55). It suggests that the mass accretion rate of V2129 Oph is stable³ to within a factor of $\simeq 2$ on both short and long timescales (i.e., weeks to years). Given the intensity of the dipole component reconstructed for V2129 Oph (equal to $B_\star \simeq 450$ G and $\simeq 150$ G at the equator in 2009 and 2005 respectively, see Sec. 5) and using a logarithmic mass accretion rate of -9.0 , we obtain that the radius r_{mag} at which the inner disc of V2129 Oph is truncated is $r_{\text{mag}} \simeq 7.2 R_\star$ and $\simeq 3.9 R_\star$ for 2009 and 2005 respectively⁴, or equivalently that $r_{\text{mag}}/r_{\text{cor}} \simeq 0.93$ and $\simeq 0.50$ at the same two epochs (using the theoretical estimates of Bessolaz et al. 2008).

³ More data collected over a longer time span are however needed to confirm that we did not catch V2129 Oph in an unusually quiet state of accretion at both epochs.

⁴ Note that our previous estimate of r_{mag} in 2005 June (Donati et al. 2007), derived from a different expression of r_{mag} and a different mass accretion rate, should be considered as obsolete and superseded by the present one.

This shows that, in 2009 July, V2129 Oph has a magnetosphere extending out to $r_{\text{mag}} \simeq r_{\text{cor}}$, where the dipole component of the field vastly dominates that of the octupole (by a factor of about 25 in field strength) even though the latter dominates the former at the stellar surface (by about a factor of 2.5 and 1.9 at the poles and equator respectively); in this situation, accretion is expected to occur naturally towards the high-latitude magnetic poles only (and not towards low-latitudes, as in a pure octupole case, e.g., Long et al. 2009). Our observations confirm that this is indeed the case, with mass accretion at the surface of the star concentrating at a magnetic colatitude smaller than 10° (see Fig. 6). In 2005 June, we find that the magnetosphere only extends to $r_{\text{mag}} \simeq 3.9 R_\star$ while at the same time the dipole field is half as strong as in 2009 with respect to the octupole component (the octupole dominating the dipole by a factor of 5 at the poles and 3.8 at the equator, at the surface of the star); we nevertheless find that the dipole still dominates the octupole at r_{mag} , but only by a factor of about 4 in field strength. We speculate that this is enough for surface accretion to concentrate mostly at magnetic poles only (rather than at low latitudes) as suggested again by observations.

Our results are in relatively good agreement with those of recent very detailed 3D MHD simulations carried out in the specific case of V2129 Oph (Romanova et al. 2010). In particular, estimates of the relative extent of r_{mag} with respect to r_{cor} and its dependence with dipole strength and accretion rate are roughly compatible. The grossly circular shape and polar location of accretion spots found in our maps is also similar to theoretical predictions when $r_{\text{mag}}/r_{\text{cor}} \gtrsim 0.7$ and differ in particular from the predicted crescent-shaped accretion regions in purely dipolar magnetospheres (e.g., Romanova et al. 2003); the accretion arcs/rings that simulations predict at lower latitudes when $r_{\text{mag}}/r_{\text{cor}} \simeq 0.5$ (i.e., as in 2005) are however not observed, for a yet unclear reason.

Balmer profiles further document the different magnetospheric accretion configurations of V2129 Oph in 2009 July and 2005 June. The standard deviation profiles clearly show that the red-shifted absorption in 2009 July occurs at significantly smaller velocities than in 2005 June (see Fig. 4). The origin of this change is not clear yet; multiple observations are needed to investigate this issue in more details. In addition, we observe that this red-shifted Balmer absorption is trailing magnetic maximum in 2009 July (by about 0.15 cycle in average, see Sec. 4), while the opposite is observed in 2005 June. We suggest it indicates that part of the accretion funnel is anchored beyond r_{cor} in 2009 July (as expected from $r_{\text{mag}} \simeq r_{\text{cor}}$) with the corresponding flux tubes lagging the main funnel as they are dragged behind by the slow Keplerian flow; since $r_{\text{mag}} \ll r_{\text{cor}}$ in 2005 June, we may logically expect an opposite situation (with the base of accretion funnels being dragged ahead of the main magnetic region by the fast Keplerian flow), in rough qualitative agreement with observations. Finally, blue-shifted Balmer emission is detected at velocities of $\simeq -170 \text{ km s}^{-1}$ in 2009 July while none was seen in 2005 June, suggesting that V2129 Oph is now triggering a significant outflow; we propose that this outflow comes from the inner disc, tracing the (small) fraction of the accreting disc material expelled outwards, as expected when $r_{\text{mag}} \simeq r_{\text{cor}}$.

We also report that the high-latitude accretion-powered

Ca II IRT excess emission spot that we detect at the surface of V2129 Oph (at phase $0.6 - 0.7$) is slightly trailing the main magnetic region as well as the accretion-powered He I emission spot (both centred at phase 0.5) by about 0.1 cycle in 2009 July (see Sec. 4), while all three regions were more or less overlapping in 2005 June. The origin of this small (but apparently real) spatial shift is not clear yet. We suspect that this phenomenon relates to the trailing accretion veils reported above, even though red-shifted Balmer absorption obviously traces a physically different magnetospheric plasma than Ca II IRT excess emission; we propose for instance that it reflects the complex temperature structure of the postshock region that results from the sheared accretion funnels. More data are obviously needed to investigate this issue in a quantitative way.

As a summarising conclusion, we propose a schematic description of how magnetic fields are likely to affect the evolution of cTTSs, and in particular their angular momentum. Our new spectropolarimetric data set on V2129 Oph shows that magnetic fields of cTTSs exhibit a large-scale structure, and in particular a dipolar component, that varies on a timescale of a few years, as a likely result of a non-stationary dynamo. In this context, magnetospheric accretion, essentially controlled by the lowest orders of the large-scale field of the protostar, is expected to reflect more or less directly changes in the magnetic topology. When the dipole component of the field is strong enough to ensure that $r_{\text{mag}} \gtrsim r_{\text{cor}}$, the protostar enters a propeller-like regime and is actively spun-down; when the dipole field gets weaker, r_{mag} shrinks back within r_{cor} and the star spins up again. Since the typical fluctuation timescale of dynamo fields (of order of years to decades) is much shorter than that of star-disc angular momentum transfer (by at least 4 orders of magnitude), the protostar ends up rotating at an average rate; this rate more or less reflects the mean dipole strength (with larger fields implying slower rotation) and mean mass accretion rate (with stronger accretion implying faster rotation) over the averaging timescale. As a result, cTTSs with masses in the range $0.5 - 1.3 M_{\odot}$ rotate slowly, their dynamo fields being strongly dipolar and axisymmetric like those of mid-M dwarfs (Morin et al. 2008); cTTSs with either lower or larger masses rotate more rapidly, being apparently less efficient at producing strong dipole fields (e.g., Donati et al. 2010a). AA Tau and BP Tau obviously belong to the first category, both hosting a dipole component stronger than 1 kG (Donati et al. 2008a, 2010b). With a radiative core growing in size rapidly, V2129 Oph is apparently no longer successful at building up a strong dipole field (or no more than for a small amount of time) and can likely no longer counteract its spin-up.

Upon completion, MaPP should be able to assess (on a small statistical sample) how well our proposed picture matches cTTSs; in particular, repeated and regular visits on a limited, well-selected subgroup, like that presented here for V2129 Oph, will be essential to address the important issue of non-stationary dynamos in low-mass protostars, to evaluate the constant and fluctuating parts of their dipolar fields, and to quantify the associated impact on their angular momentum evolution.

ACKNOWLEDGEMENTS

This paper is based on observations obtained at the Canada-France-Hawaii Telescope (CFHT), operated by the National Research Council of Canada, the Institut National des Sciences de l'Univers of the Centre National de la Recherche Scientifique of France and the University of Hawaii. The “Magnetic Protostars and Planets” (MaPP) project is supported by the funding agencies of CFHT and TBL (through the allocation of telescope time) and by CNRS/INSU in particular, as well as by the French “Agence Nationale pour la Recherche” (ANR). We thank an anonymous referee for suggesting various improvements to the paper, and the CFHT/QSO and TBL staff for their efficiency at collecting data. SGG acknowledges support by the Science and Technology Facilities Council [grant number ST/G006261/1].

REFERENCES

- André P., Basu S., Inutsuka S.-i., 2008, ArXiv e-prints
 Bessell M. S., Castelli F., Plez B., 1998, *A&A*, 333, 231
 Bessolaz N., Zanni C., Ferreira J., Keppens R., Bouvier J., 2008, *A&A*, 478, 155
 Bouvier J., Alencar S. H. P., Harries T. J., Johns-Krull C. M., Romanova M. M., 2007, in Reipurth B., Jewitt D., Keil K., eds, *Protostars and Planets V Magnetospheric Accretion in Classical T Tauri Stars*. pp 479–494
 Bouvier J., Appenzeller I., 1992, *A&AS*, 92, 481
 Bouvier J., Chelli A., Allain S., Carrasco L., Costero R., Cruz-Gonzalez I., Dougados C., Fernández M., Martín E. L., Ménard F., Mennessier C., Mujica R., Recillas E., Salas L., Schmidt G., Wichmann R., 1999, *A&A*, 349, 619
 Cieza L. A., Schreiber M. R., Romero G. A., Mora M. D., Merin B., Swift J. J., Orellana M., Williams J. P., Harvey P. M., Evans N. J., 2010, *ApJ*, 712, 925
 Donati J., Landstreet J. D., 2009, *ARA&A*, 47, 333
 Donati J., Skelly M. B., Bouvier J., Gregory S. G., Grankin K., Jardine M. M., Hussain G. A. J., Ménard F., Dougados C., Unruh Y., Mohanty S., Aurière M., Morin J., Farès R., and the MaPP collaboration 2010b, *MNRAS*, in press (arXiv:1007.4407)
 Donati J., Skelly M. B., Bouvier J., Jardine M. M., Gregory S. G., Morin J., Hussain G. A. J., Dougados C., Ménard F., Unruh Y., 2010a, *MNRAS*, 402, 1426
 Donati J.-F., 2003, in Trujillo-Bueno J., Sanchez Almeida J., eds, *Astronomical Society of the Pacific Conference Series Vol. 307 of Astronomical Society of the Pacific Conference Series, ESPaDOnS: An Echelle Spectropolarimetric Device for the Observation of Stars at CFHT*. pp 41–+
 Donati J.-F., Collier Cameron A., Petit P., 2003, *MNRAS*, 345, 1187
 Donati J.-F., Howarth I. D., Jardine M. M., Petit P., Catala C., Landstreet J. D., Bouret J.-C., Alecian E., Barnes J. R., Forveille T., Paletou F., Manset N., 2006, *MNRAS*, 370, 629
 Donati J.-F., Jardine M. M., Gregory S. G., Petit P., Bouvier J., Dougados C., Ménard F., Cameron A. C., Harries T. J., Jeffers S. V., Paletou F., 2007, *MNRAS*, 380, 1297
 Donati J.-F., Jardine M. M., Gregory S. G., Petit P., Paletou F., Bouvier J., Dougados C., Ménard F., Cameron A. C., Harries T. J., Hussain G. A. J., Unruh Y., Morin

- J., Marsden S. C., Manset N., Aurière M., Catala C., Ale-
cian E., 2008a, MNRAS, 386, 1234
- Donati J.-F., Moutou C., Farès R., Bohlender D., Catala
C., Deleuil M., Shkolnik E., Cameron A. C., Jardine
M. M., Walker G. A. H., 2008b, MNRAS, 385, 1179
- Donati J.-F., Semel M., Carter B. D., Rees D. E., Collier
Cameron A., 1997, MNRAS, 291, 658
- Fang M., van Boekel R., Wang W., Carmona A., Sicilia-
Aguilar A., Henning T., 2009, ArXiv e-prints
- Furlan E., Watson D. M., McClure M. K., Manoj P., Es-
paillet C., D'Alessio P., Calvet N., Kim K. H., Sargent
B. A., Forrest W. J., Hartmann L., 2009, ApJ, 703, 1964
- Grankin K. N., Bouvier J., Herbst W., Melnikov S. Y.,
2008, A&A, 479, 827
- Gregory S., Flaccomio E., Argiroffi C., Bouvier J., Donati
J.-F., Feigelson E., Getman E., Hussain G., Jardine M.,
Walter F., 2009, in High Resolution X-ray Spectroscopy:
Towards IXO Multi-wavelength observing of a forming
solar-like star
- Johns-Krull C. M., 2007, ApJ, 664, 975
- Kurucz R., 1993, CDROM # 13 (ATLAS9 atmospheric
models) and # 18 (ATLAS9 and SYNTHE routines, spec-
tral line database). Smithsonian Astrophysical Observa-
tory, Washington D.C.
- Loinard L., Torres R. M., Mioduszewski A. J., Rodríguez
L. F., 2008, ApJL, 675, L29
- Long M., Romanova M. M., Lamb F. K., 2009, ArXiv e-
prints
- Mohanty S., Jayawardhana R., Basri G., 2005, ApJ, 626,
498
- Morin J., Donati J.-F., Petit P., Delfosse X., Forveille T.,
Albert L., Aurière M., Cabanac R., Dintrans B., Fares
R., Gastine T., Jardine M. M., Lignières F., Paletou F.,
Ramirez Velez J. C., Théado S., 2008, MNRAS, 390, 567
- Natta A., Testi L., Muzerolle J., Randich S., Comerón F.,
Persi P., 2004, A&A, 424, 603
- Romanova M., Utsyugova G., Koldoba A., Wick J.,
Lovelace R., 2003, ApJ, 595, 1009
- Romanova M. M., Long M., Lamb F. K., Kulkarni A. K.,
Donati J., 2010, MNRAS, in press (arXiv:0912.1681)
- Siess L., Dufour E., Forestini M., 2000, A&A, 358, 593